Influences of lateral boundary forcings on the 2020 extreme Meiyu in the Yangtze-Huaihe River valley

Xiaoyu Zhu
National University of Defense Technology
Yijia Hu (lgdxhuyijia@163.com)
National University of Defense Technology
Xuguang Sun
Nanjing University
Zhong Zhong
National University of Defense Technology
Yao Ha
National University of Defense Technology

Research Article

Keywords: Extreme Meiyu, Regional Climate Model, Lateral boundary forcings, Boreal summer intraseasonal oscillation, Upper-level subtropical jet, Western Pacific subtropical high

Posted Date: November 29th, 2022

DOI: https://doi.org/10.21203/rs.3.rs-2255232/v1

Abstract

In this study, a Regional Climate Model (RegCM4.6) is employed to simulate the extreme Meiyu in the Yangtze-Huaihe River valley (YHRV) from June to July 2020. The influences of lateral boundary forcings in different directions on the 2020 Meiyu are explored through a series of sensitivity experiments with realistic or climatological lateral boundary conditions in the south, north and east directions, respectively. The results show that the 2020 Meiyu occurs under unique atmospheric forcings, and if all lateral boundary conditions are replaced by climatological mean state, heavy rainfall will not occur. Specifically, the south atmospheric signals provide moisture and heat for the occurrence of Meiyu. The atmospheric longwave activities in the north bring cold air to YHRV which can lift the warm air, provide instability conditions, and make the distribution of Meiyu similar to the teleconnection pattern of summer precipitation in East Asia. The western Pacific subtropical high (WPSH) in the east is important in anchoring the rainband locations in YHRV. In addition, the contributions of anomalous atmospheric signals in different directions change with time. Before June 10, the WPSH mainly contributes to the Meiyu evolution. From June 11 to July 3, the combined effects of forcings in the south and north are dominant. From July 3 to July 10, the cold air from the north plays a major role. After July 10, the 2020 atmospheric circulation conditions and Meiyu evolution are similar to the climatological mean state.

1. Introduction

The typical rainy season of the East Asian summer monsoon (EASM), which generally begins in mid-June and ends in mid-July, is known as the “Meiyu” in China, “Baiu” in Japan and “Changma” in the Koreas (Saito 1985, Tao and Chen 1987, Oh et al. 1997). The precipitation that occurs during the Meiyu period accounts for most of the total precipitation in the whole year and often results in severe flooding in the Yangtze-Huaihe River valley (YHRV) (Ding 1992, Ding and Chan 2005). Therefore, it is very important to deepen the understanding of the occurrence and maintenance mechanisms of Meiyu and thus make accurate predictions (Chen et al. 2017, Ding et al. 2020, Guan et al. 2020).

In the summer of 2020, a record-breaking Meiyu rainfall, featuring an early onset, delayed retreat, abundant precipitation and frequent heavy rainstorm processes, appeared in YHRV, which was systematically analyzed by Ding et al. (2021). The accumulated precipitation during the summer of 2020 broke historical records since 1961, causing economic losses of $11.75 billion and the deaths of 219 people (Wang et al. 2021). Many recent studies emphasized the remote effect of the warm Indian Ocean or the North Atlantic Oscillation (NAO) on this extreme Meiyu. Takaya et al. (2020) and Ding et al. (2021) emphasized the role of Indian Ocean warming in enhancing precipitation by stretching the western Pacific subtropical high (WPSH) to the southwest, and it also favors exceptionally persistent and quasi-stationary Madden-Julian oscillation (MJO) activities, which is an important reason for this extreme rainfall (Zhang et al. 2021). In addition, Liu et al. (2020) considered that the Meiyu front regulated by NAO was responsible for this unexpected extreme Meiyu event. However, the contributions of anomalous atmospheric signals in different directions at different period haven’t been well analyzed.

The Meiyu front is a planetary-scale, quasi-stationary front formed by the interaction between warm and wet air from low latitudes and cold and dry air from middle and high latitudes (Ninomiya 1984, 2000, Ding 2007, Ding et al. 2021), which is influenced by factors from different directions (Mao and Wu 2006, Ninomiya and Shibagaki 2007, Liu et al. 2019, Ding et al. 2020). A low-level southwesterly jet on the south side of the YHRV provides sufficient moisture for the summer rainfall in East China (Zhang and Sumi 2002, He et al. 2007). The northward leap of the upper-level westerly jet, which is located on the north side of the YHRV, is a precursor to the onset of Meiyu (Li et al. 2004, Li and Zhang 2014), and the large-scale environmental forcings caused by the East Asian subtropical jet are important reasons for the occurrence and maintenance of the Meiyu rainband (Sampe and Xie 2010). On the east side of the YHRV, the location and intensity of the WPSH is an important circulation background for Meiyu, and the locations of the rainbands depend largely on the position of the WPSH (Lu et al. 2005, Yang et al. 2010, Liu et al. 2012, Sun et al. 2021). In addition, on the south side of the YHRV, a quasi-biweekly oscillation (QBWO) is presented over the Indian Ocean and South China Sea, which also has a close relationship with Meiyu (Kemball-Cook and Wang 2001, Chen et al. 2015, Song et al. 2016, Ding et al. 2020). The QBWO influences the onset, withdrawal, and active/break spells of Meiyu over the YHRV (Annamalai and Slingo 2001, Seo et al. 2007), which shows the close connection between external anomalous atmospheric forcings and the internal dynamic processes of the Meiyu. On the west side of the YHRV, the Tibetan Plateau vortices and southwest vortices are important rainfall producers for Meiyu when they emigrate from where they originated (Huang et al. 2015, Li et al. 2020). Therefore, the factors affecting this extreme 2020 Meiyu are complex, and further research is needed to reveal the role of various factors from different directions of the YHRV on this record-breaking rainfall.

The article is organized as follows. In section 2, the model, datasets and methods are presented. The distribution and evolution of rainfall due to different influencing factors are analyzed in section 3 and the conclusions are presented in section 4.

2. Model, Datasets And Methods

The model used in this study is the Regional Climate Model version 4.6 (RegCM4.6) developed by the Abdus Salam International Center for Theoretical Physics (ICTP) (Giorgi et al. 2011), which has a hydrostatic dynamic core on an Arakawa B horizontal grid. RegCM4.6 is widely used because of its various applications, including studies of modern-day climate simulation, land-atmosphere interactions, climate change projections and further model developments (Giorgi et al. 1999, Chen et al. 2002, Gao et al. 2017).

To simulate the Meiyu in the YHRV in 2020, the Lambert projection is adopted in this study with the center located at 32°N, 110°E. Figure 1 shows the model domain used in this study and the corresponding geopotential height. The horizontal resolution is 50 km, and the number of horizontal grid points is 100 (west-east) × 100 (south-north), while 23 vertical levels are used within the sigma coordinate. The buffer zone is ten grid points for each lateral boundary. The initial and lateral boundary conditions used for driving the RegCM4.6 model are obtained from the National Centers for Environmental Prediction and the

National Center for Atmospheric Research (NCEP-NCAR) reanalysis data, with a resolution of 2.5° × 2.5°. The model is initialized at 0000 UTC on 1 May 2020 and ends at 0000 UTC on 1 August 2020, and the first month is used as the spin-up period and excluded from subsequent analysis. The time step is 120 seconds and the model outputs are produced every 6 hours.

The physical parameterizations used in this study include the nonlocal planetary boundary layer scheme of Holtslag (Holtslag et al. 1990), the ocean flux scheme of Zeng (Zeng et al. 1998), the cumulus scheme of Emanuel (Emanuel 1991) and the land surface scheme of Community Land Model version 4.5 (CLM4.5) (Lawrence et al. 2011) with a time step of 600 seconds.

The observational precipitation data are derived from the Integrated Multi-satellite Retrievals for Global Precipitation Measurement Mission (IMERG), version 6 (Huffman 2020), with a resolution of 0.1° × 0.1° for the period from June to July 2020. The reanalysis data from NCEP-NCAR and precipitation data from IMERG are used as observations to evaluate the model outputs. To unify the spatial resolutions of all the data, the precipitation data and model outputs are interpolated into the grids with horizontal resolution of 2.5° × 2.5°.

The boundary conditions of the control experiment (Exp_Control) use the realistic reanalysis data in 2020, and seven sensitivity experiments are set up (see Table 1 and Fig. 2). Exp_30ave uses the 30-year climatological average data from 1991 to 2020 as the boundary conditions. The other sensitivity experiments replace the boundary condition of the Exp_30ave at the south boundary (Exp_South), the north boundary (Exp_North), the south and north boundaries (Exp_South&North), the east boundary (Exp_East), the south and east boundaries (Exp_South&East), and the north and east boundaries (Exp_North&East) with 2020 realistic data, respectively, while the other boundaries are consistent with the Exp_30ave. The specific experimental configurations are shown in Table 1.

Table 1
Model configurations for the 7 experiments

Exp	Model configuration
Exp_Control	Using 2020 realistic atmospheric conditions as boundary conditions
Exp_30ave	Using 30-year average data as boundary conditions
Exp_South	Adding 2020 realistic atmospheric conditions to the south boundary based on Exp_30ave
Exp_North	Adding 2020 realistic atmospheric conditions to the north boundary based on Exp_30ave
Exp_South&North	Adding 2020 realistic atmospheric conditions to the south and north boundaries based on Exp_30ave
Exp_East	Adding 2020 realistic atmospheric conditions to the east boundary based on Exp_30ave
Exp_South&East	Adding 2020 realistic atmospheric conditions to the south and east boundaries based on Exp_30ave
Exp_North&East	Adding 2020 realistic atmospheric conditions to the north and east boundaries based on Exp_30ave

3. Results Analysis

3.1 The distribution and evolution of rainfall

The extreme Meiyu in 2020 is produced under specific circulation conditions (Ding et al. 2021). Figure 3 shows the observed circulation distribution of the 30-year climatological mean state from 1991 to 2020, the state in 2020, and the bias between them. The southwesterly jet at 850 hPa in June-July 2020 is weaker than the climatological mean state, which only reaches the YHRV (Figs. 3a and 3b). The southerly anomalies converge with the northerly anomalies in YHRV, favoring the convergence at lower levels and the long-term maintenance of Meiyu (Fig. 3c). In addition, the upper-level westerly jet at 200 hPa in the summer of 2020 is also stronger than the climatological mean state (Figs. 3g, 3h and 3i), which means large horizontal temperature gradient with strong cold air from the north and warm air from the south meet in YHRV (Li and Zhang 2014; Xu et al. 2022), and this favors the occurrence of the 2020 extreme Meiyu. In the following part, the effects of different lateral boundary forcings on the extreme 2020 Meiyu in the YHRV are specifically analyzed through comparisons between observations and different sensitivity experiments.

From the observed precipitation distribution in June-July 2020 (Fig. 4a), the precipitation intensity of the 2020 Meiyu appears to be very strong and the maximum value rainfall center exceeds 20 mm per day. The main rainband is located along the lower and middle reaches of the Yangtze River near 30°N, with an east-west zonal distribution. Comparing the simulated precipitation of Exp_Control (Fig. 4b) and the

observations, it can be found that the Exp_Control can well reproduce the characteristics of the Meiyu rainfall distribution, but the simulated precipitation intensity is weaker than the observations. The weak rainfall bias may due to the hydrostatic dynamic core of RegCM4.6 (Giorgi et al. 2011), it cannot well describe the intense precipitation produced by local non-hydrostatic meso-small scale system in Meiyu front.

Driven by the 30-year climatological average reanalysis data, the summer rainfall distribution simulated by Exp_30ave (Fig. 4d) is relatively similar to the observed 30-year climatological averaged condition (Fig. 4c), that is, there is more precipitation in South China and North China but less precipitation in the YHRV. The precipitation simulated by Exp_30ave shows a "+-+" wavelike pattern.

To avoid the impacts of the systematic weak bias simulated by RegCM4.6, the simulated rainfall of Exp_Control is assumed to be accurate. The differences between Exp_Control and other sensitivity experiments can be obtained by subtracting the Exp_Control results from sensitivity experiments results to quantify the contributions of the lateral boundary forcings in different directions. From the precipitation bias between Exp_30ave and Exp_Control (Fig. 5a), it can be found that the precipitation bias shows a "+-+" pattern, with a strong negative deviation center in the YHRV and a positive center in North China and South China. These results indicate that the extreme Meiyu is produced under special atmospheric forcings in 2020, and if these anomalous atmospheric signals are removed, heavy rainfall will not occur in the YHRV.

Summer rainfall in China is closely related to the atmospheric anomalies from the south ocean, such as the summer monsoon and the water vapor transported by the monsoon, convection over the tropical ocean, and the boreal summer intraseasonal oscillation (BSISO) transmitted from south to north (Kemball-Cook and Wang 2001, Zhang and Sumi 2002, He et al. 2007, Chen et al. 2015, Song et al. 2016, Ding et al. 2020). After adding the 2020 realistic boundary forcings to the south boundary, it can be found that little precipitation occurs over most parts of China (Fig. 4e). The bias between Exp_South and Exp_Control shows large negative deviations, especially in the YHRV (Fig. 5b). The southwesterlies from the south ocean can transport moisture and heat to YHRV. However, without the cold air from the north, the water vapor in the air cannot be lifted to produce precipitation.

Frequent trough and ridge activities in upper-level westerlies north of YHRV can bring cold air to the YHRV, lift the moist air, and result in thermal instability for the occurrence of precipitation, which is important for the maintenance of Meiyu in the YHRV (Li et al. 2004, Sampe and Xie 2010). Therefore, the results of Exp_North show that after adding the realistic atmospheric forcing in the north boundary, the precipitation increases significantly compared to both Exp_South and Exp_30ave, with large precipitation center locates in South China, the lower reach of the Yangtze River, and parts of North China (Fig. 4f). From the precipitation bias between Exp_North and Exp_Control (Fig. 5c), it can be found that the distribution of precipitation bias shows a "+-+-+" pattern from south to north in the meridional direction, indicating that when the cold air from the north is active, it also makes the teleconnection pattern similar to the distribution of summer precipitation in East Asia.

If the 2020 realistic south and north anomalous atmospheric signals are added to the lateral boundary condition at the same time (Exp_South&North), large amount of precipitation occurs in North China, and some precipitation appears in the Yangtze River basin (Fig. 4g). The bias between Exp_South&North and Exp_Control further shows that the precipitation caused by the combined effect of 2020 realistic south boundary forcing and north boundary forcing is still weak in the YHRV. The location of the main rainband is in North China, not in the YHRV (Fig. 5d). Both the Exp_South and Exp_South&North add the 2020 realistic south boundary forcing, which is characterized as weaker southwesterlies than the climatological mean state (Fig. 3). However, the weak southwesterlies alone does not result in heavy rainfall in the YHRV but rather results in less precipitation in both the YHRV and South China.

The WPSH is located in east China and is one of the important systems influencing the Meiyu rainfall (Lu et al. 2005, Yang et al. 2010, Liu et al. 2012, Sun et al. 2021). After adding the 2020 realistic east boundary forcing, it can be found that the Exp_East can well simulate the location and intensity of the WPSH as well as the rainband. The northeast-southwest rainband is mainly located in South China and the middle and lower reaches of the Yangtze River (Fig. 4h). This result indicates that the WPSH is very important for anchoring the Meiyu rainband location in 2020. Strong intensity and south location of WPSH often correspond to the strong Meiyu in YHRV (Fig. 3). From the distribution of the bias between Exp_East and Exp_Control (Fig. 5e), positive bias can be seen in the lower reach of the Yangtze River, south China, and North China, indicating that the Exp_East produce excessive precipitation in South China and North China. Negative bias still exists in the middle reach of the Yangtze River.

Exp_South&East uses both the realistic south boundary forcing and east boundary forcing. From the results of Exp_South&East (Fig. 4i), it can be found that the precipitation in South China is significantly reduced and the northeast-southwest rainband appears in the middle and lower reaches of the Yangtze River. The distribution of precipitation bias between Exp_South&East and Exp_Control (Fig. 5f) that the south boundary forcing can decrease the precipitation in South China, and produce a northeast-southwest rainband rather than an east-west rainband as the observation and Exp_Control.

After adding both the 2020 realistic north and east boundary forcing (Exp_North&East), the simulated precipitation in South China is further reduced and the rainband shifts northwards. In addition, the simulated rainband shows the same east-west zonal distribution characteristics as the observations and Exp_Control (Figs. 4i and 5g). These results indicate that the combination of the active cold air from the north and strong WPSH can generate an east-west zonal rainband in the Yangtze River basin. Therefore, the cold air from the north is important for the formation of precipitation, and the location of WPSH determines the location of the rainbands.

By comparing the precipitation bias between sensitivity experiments and Exp_Control, for the extreme Meiyu in summer 2020, the different lateral boundary forcings from the south, north and east sides are key factors for the formation of 2020 Meiyu. The weak warm moist southwesterlies can reduce precipitation in South China and provide moisture and heat for heavy rainfall. However, the south boundary forcing alone cannot generate much rainfall without the lift by cold air and thermal instability

conditions. In addition, the active troughs and ridges as well as cold air activities in the north provide lifting and instability conditions for the occurrence of precipitation. The WPSH in the east can anchor the position of the rainband.

We can also infer the contributions of different lateral boundary forcings in the precipitation evolution by comparing the simulated precipitation evolutions of sensitivity experiments with the Exp_Control. Figure 6 shows the time-latitude profiles of the zonal-averaged precipitation in 107–122°E during June and July. From the observed evolution of precipitation (Fig. 6a), an obvious QBWO of Meiyu is presented in the Yangtze River basin, and the rainband position oscillates north and south around 30°N. By comparing Exp_Control (Fig. 6b) and the observations, it can be found that the Exp_Control can basically simulate the evolution of rainband location and intensity under the 2020 realistic atmospheric forcings, but the precipitation simulated by Exp_Control is weaker than the observations after July 15, indicating that the physical processes causing the strong rainfall in YHRV after July 15 are poorly simulated by the model.

By comparing the Exp_30ave with Exp_Control, there are no significant QBWO of the rainfall in the Yangtze River basin until July 10 (Fig. 6c). Between June 13 and July 5, precipitation is concentrated in South China and South China Sea. However, Exp_30ave can reproduce the rainband evolution after July 10, with two northward movements and one southward movement, indicating that the atmospheric conditions after July 10 in 2020 are similar to the climatological mean state, resulting in the similar rainband evolution in 2020 to the climatological mean state. However, the two northward shifts simulated by Exp_30ave reach further north than the observations, indicating that the southwesterlies from the south in the climatological mean state is stronger than that in 2020, and that the WPSH can jump to a more northerly position than that in 2020 (Fig. 3).

The results of Exp_South (Fig. 6d) shows that if only the realistic south boundary forcing is added, there is nearly no precipitation occurring in the Yangtze River basin, and the precipitation does not have characteristics of QBWO before July 15. The rainband moves southward during 15–20 July, then moves northward after 20 July, which is consistent with the Exp_30ave (Fig. 6c), indicating that this precipitation process can be generated even without the atmospheric anomalies in 2020.

After adding the realistic north boundary forcing, the precipitation simulated by Exp_North significantly increases and shows an obvious QBWO characteristics. However, the location of the rainbands is more northward than the observation before June 20, and the oscillation feature is different from those of Exp_Control and the observations. The southward shift of the rainband simulated by Exp_North from July 3 to July 10 is nearly the same as Exp_Control, indicating that the anomalous atmospheric forcing in the north plays an important role in the precipitation evolution during this period.

If both the realistic north and south boundary forcings are added at the same time, it can be found that the simulated precipitation by Exp_South&North is larger than the Exp_North, and the north-south oscillation of the precipitation is closer to the observations than the Exp_North (Fig. 6f). The pattern correlation coefficient between the simulated precipitation evolution of Exp_South&North and Exp_Control is the highest among all experiments (Fig. 7), so it can be inferred that the north-south oscillation of the

precipitation is mainly caused by the interplay of warm moist air from the south and the cold air from the north. Many studies have demonstrated the combined effect of the warm moist air from the south and the cold air from the north is important for the QBWO of summer precipitation (Chen et al. 2015, Ding et al. 2020). However, due to the lack of the realistic WPSH's forcing in 2020, the rainband simulated by Exp_South&North locates more northward than observation, with precipitation mainly concentrated in north of 30°N (Fig. 6f).

By comparing the Exp_East (Fig. 6g) with Exp_Control (Fig. 6b) and the observations (Fig. 6a), it can be found that the southward movement of the rainband is consistent with the observation before June 10. This result suggests that the WPSH plays a major role in the precipitation evolution before June 10. However, with only the east boundary forcing, Exp_East simulates no precipitation oscillations in YHRV from June 11 to July 3. The north-south oscillation of the rainband after July 10 simulated by Exp_East is similar to Exp_30ave, further indicating that the atmospheric conditions during this period are close to the 30-year climatological mean state and no atmospheric forcing in any one direction plays a dominant role.

After adding both the south and east boundary forcings, the precipitation oscillations simulated by Exp_South&East (Fig. 6h) are very close to those simulated by Exp_Control (Fig. 6b), and it has the second highest pattern correlation coefficient (Fig. 7). The pattern correlation coefficients of Exp_South&East and Exp_South&North are high because both the two experiments have realistic south boundary forcing, indicating that the south atmospheric signals are crucial for the QBWO of the extreme Meiyu.

Figure 6i shows that the simulated rainband by Exp_North&East experiences a southward process and a northward process before June 17, and the intensity of precipitation is strong in the YHRV, suggesting that the cold air from the north together with the southeasterly warm and moist air from the south of the WPSH are the main reasons for the occurrence of strong rainfall during this period. However, Exp_North&East fails to simulate the strong rainfall in YHRV and its QBWO from June 18 to July 3, and the simulated rainband is more northward, indicating that the anomalous rainfall in this period must be produced by the combined effect of anomalous atmospheric signals from the north, south and east.

In a whole, Fig. 7 shows that the contributions of the anomalous atmospheric forcings in different directions change with time. Among them, the east boundary forcing contributes to the precipitation evolution before June 10. The precipitation oscillation process from June 11 to July 3 is mainly caused by the combined effect of south and north atmospheric anomalies forcings. From July 3 to July 10, the north anomalous atmospheric forcings are important in the southward movement of the rainband. The atmospheric conditions in 2020 are similar to the climatological mean state after July 10, so the rainband evolution in 2020 is also similar to the climatological mean state, and no anomalous atmospheric forcing in any direction plays a leading role during this period.

3.2 Relationship between southwesterly jet and Meiyu

The summer rainfall in East China is closely related to the EASM, and the evolution and strength of EASM can lead to precipitation anomalies (He et al. 2007; Ding et al. 2021). Figure 8 shows the time-latitude profiles of the 850 hPa meridional wind, horizontal wind and divergence of the vertically integrated water vapor transported from the surface to 300 hPa averaged over 107°-122°E during June-July. From the observations (Fig. 8a), it can be seen that the large value center of the southerlies is stable in the south of 30°N. Its intensity and evolution show an obvious characteristic of QBWO during June and July 2020. The convergence of water vapor, which is located in the north of the large value area of the southerly wind, provides favorable dynamic lifting conditions for heavy rainfall. The monsoon southwesterlies from the south and the cold air from the north keep converging near 30°N, leading to the super Meiyu in 2020. By comparing Exp_Control (Fig. 8b) with the observations, it can be found that the Exp_Control can basically reproduce the evolution of the southwesterlies, but the large value region of the southerlies extends more northward than observations after July 15, resulting in a more northward rainband and less Meiyu rainfall during this period.

The monsoon southwesterlies simulated by Exp_30ave (Fig. 8c) is stronger and extends further more northward than that simulated by Exp_Control, resulting in the convergent zone of water vapor and the rainband move northward of 30°N by June 21. From June 21 to July 5, the southerlies intensity simulated by Exp_30ave is weak, making the rainband move southward. After July 10, the wind evolution simulated by Exp_30ave is similar to Exp_Control, so the simulated rainband evolutions are also consistent with the Exp_Control, further indicating that the atmospheric circulation evolution after July 10 in 2020 is similar to the climatological mean state.

Adding the realistic boundary forcings in south or north direction alone cannot reproduce the evolution of the monsoon southwesterlies. For example, the Exp_South simulates strong southerlies, which extends northerly, resulting in a more northerly rainband than observation. After July 15, the monsoon southwesterlies evolution of Exp_South is close to Exp_Control, indicating that the atmospheric anomalies are also close to the climatological mean state during this period (Fig. 8d). The simulated southwesterlies by Exp_North extend more northward and has weaker intensity than Exp_Control in June (Fig. 8e), resulting in a north rainband in June (Fig. 6e). The evolution of monsoon southwesterlies in July simulated by Exp_North is similar to the Exp_Control, thus the rainband evolution is also be well reproduced by Exp_North. The realistic south and north boundary forcings together help the Exp_South&North to produce a reasonable evolution of the southwesterlies, which makes the simulated evolution of the rainband by Exp_South&North the best in all the sensitivity experiments. Thus, the interaction between cold air from the north and the warm moist air from the south is very important for the maintenance and oscillation of rainband.

Exp_South&East (Fig. 8h) and Exp_North&East (Fig. 8i), Exp_East (Fig. 8g) all have realistic east boundary forcing. From the results of the three experiments, it can be found that the east boundary forcing can help control the strong southerlies stay south of the 30ºN and the convergence zone of the northerlies and southerlies maintained near the 30ºN. However, without the north boundary forcing and the south boundary forcing, the simulated evolution of the southwesterlies by Exp_East deviate from the

Exp_Control in June, further indicating that both the north boundary forcing and south boundary forcing are very important to the intraseasonal oscillation of monsoon southwesterlies.

By analyzing the 850 hPa atmospheric circulation deviations between sensitivity experiments and the Exp_Control (Fig. 9), it can be found that the circulation deviation has a south-to-north distribution of "cyclone", "anticyclone", and "cyclone", thus causing the precipitation deviation to show "+-+" characteristics from south to north (Fig. 5). The anomalous atmospheric forcings can meridionally distribute the anomalous precipitation in 2020, similar to the teleconnection pattern of the summer precipitation in East Asia (figure omitted).

3.3 Relationship between WPSH and Meiyu

Figure 10 shows the time-latitude profiles of the zonal-averaged ridgeline of the WPSH and 500 hPa vorticity in June-July, where the ridgeline of the WPSH represents the position of the WPSH. The negative vorticity region in the south represents the region controlled by WPSH. As shown in Fig. 10a, the north-south movement of the WPSH is basically consistent with the north-south movement of the Meiyu rainband (Fig. 6a), and has obvious characteristics of QBWO. By comparing Exp_Control with the observation, it can be found that the Exp_Control can basically reproduce the northward and southward movements of the WPSH (Fig. 10b). The evolution of the positive vorticity is consistent with the northward and southward movements of the rainband (Fig. 6b). After July 15, the simulated WPSH and negative vorticity region by Exp_Control are more northward than the observation, resulting in a weak and northerly Meiyu rainband during this period.

The WPSH simulated by Exp_30ave is more northward than that in 2020 (Fig. 10c), which is consistent with the climatological averaged state (Fig. 3). However, the WPSH simulated by Exp_30ave is closer to Exp_Control and the observations after July 10, further indicating that the atmospheric state is close to the climatological mean state after July 10. Without the east realistic boundary forcing, the Exp_South (Fig. 10d), Exp_North (Fig. 10e), and Exp_South&North (Fig. 10f) cannot simulate the position of the WPSH well before July 10. They produce a more northerly WPSH, resulting in a northerly rainband. In contrast, in the control of the realistic east boundary forcing, the Exp_East (Fig. 10g), Exp_South&East (Fig. 10h) and Exp_North&East (Fig. 10i), can greatly improve the simulation of the WPSH. Among them, the simulated evolution of the WPSH in Exp_North&East is closest to Exp_Control and observation, with the ridgeline stabilized near 25ºN, suggesting that the interplay of north and east atmospheric signals play a key role in the evolution of the WPSH and Meiyu rainband.

3.4 Relationship between the upper-level westerly jet and Meiyu

Figure 11 shows the time-latitude profiles of the zonal-averaged 200 hPa zonal winds, geopotential height and divergence in June-July. As shown in the observations (Fig. 11a), the subtropical westerly jet is maintained between 30°N and 40°N from the beginning of June to July 20, with a constant strong

intensity. The strong subtropical westerly jet is related with the continuous convergence of cold air from the north and warm air from the south, which intensify the south-north temperature gradient. The south side of the jet is the positive divergent zone which can provide good lifting conditions for precipitation, and the evolutions of both the positive divergence and the rainband (Fig. 6a) are basically consistent. Moreover, the position of the South Asia High is relatively stable and maintained south of 30°N. The weak jet simulated by Exp_Control makes the total precipitation simulated by Exp_Control also has a weak bias in intensity (Fig. 11b).

If only the realistic south boundary forcing is added, the westerly jet simulated by Exp_South is weak before June 20, so there is no precipitation occurring in the YHRV during this period. Between June 20 and July 10, the simulated westerly jet by Exp_South is stronger but located more northward than observation, resulting in no precipitation in YHRV. According to the previous analysis, the anomalous atmospheric conditions in 2020 are similar to the climatological mean state after July 10, so the simulated westerly jet by Exp_South is weak as the Exp_Control and observation (Fig. 11d).

If only the north boundary forcing is included (Exp_North), although the subtropical jet is close to the north boundary and the realistic atmospheric forcing can diffuse from the north boundary through the buffer zone to the interior of the region, Exp_North cannot reproduce the intensity and evolution of the subtropical jet, and the simulated subtropical jet is much weaker than that in Exp_Control (Fig. 11e). These results suggest that there is a systematic interaction between the north cold air, south warm air and Meiyu rainfall. The upper-level jet is in the subtropical frontal region with large north-south temperature gradient. The south boundary forcing in Exp_North is the climatological mean state, leading to a strong monsoon southwesterlies and a weak Meiyu. The weak precipitation releases less latent heat of condensation, causing a weak temperature gradient and weak westerly jet in Exp_North (Fig. 11e).

Without the realistic north boundary forcing, the Exp_East and the Exp_South&East cannot well simulate the westerly jet. Among all sensitivity experiments, only Exp_South&North (Fig. 11h) and Exp_North&East (Fig. 11i) can reproduce the intensity and evolution of the upper-level jet well, suggesting that the north boundary forcing combined with south or east boundary forcing can reproduce the continuous convergence of the north cold air and south warm air, which intensifies the temperature gradient and favors the strong westerly jet and Meiyu. Without the north atmospheric forcing, the westerly jet is weak.

4. Conclusions

In this study, we focus on the extreme Meiyu process in the YHRV from June to July 2020. The NCEP-NCAR reanalysis data were used as the large-scale boundary forcings to drive RegCM4.6. The contributions of lateral boundary forcings in different directions were explored through a series of sensitivity experiments with the realistic or climatological lateral boundary conditions in the south, north and east directions, respectively. The main conclusions are given as follows.

Compared with the 30-year climatological mean state, the overall atmospheric circulation in the summer of 2020 shows the following characteristics: First, the monsoon southwesterlies is weak. Second, the cold

air from the north is active. Third, the WPSH is strong and located to the south. Driven by the 2020 realistic reanalysis data, Exp_Control can well reproduce the distribution of Meiyu in June-July, but the intensity of the simulated precipitation is weak, indicating that the RegCM4.6 with a hydrostatic dynamic core remains deficient in simulating the local non-hydrostatic meso-small scale system. The simulated precipitation driven by 30-year averaged reanalysis data is very similar to the observed 30-year climatological averaged precipitation, with a "+-+" tripolar distribution characteristic, that is, less precipitation in the YHRV and more precipitation in North China and South China. The results indicate that the extreme Meiyu in 2020 is produced under the special atmospheric forcings in 2020, and if all these anomalous atmospheric signals are removed, the Yangtze River basin will not experience this heavy precipitation.

The monsoon southwesterlies can provide moisture and heat conditions for the occurrence of Meiyu, and the weak monsoon southwesterlies tends to cause less precipitation in South China. However, if only the 2020 realistic south boundary forcing is added, little precipitation occurs over most parts of China. Therefore, the cooperation of lifting conditions and atmospheric instability conditions provided by the cold air from the north and the strong and south WPSH is critical for the extreme Meiyu. The persistent activities of upper-level atmospheric troughs and ridges in the north and the resulting cold air are important for the extreme Meiyu in 2020. They not only provide lifting and thermal instability conditions for the occurrence of this extreme Meiyu, but also make the precipitation present a wave like distribution. The east WPSH plays a major role in anchoring the rainband location. The southerly and strong WPSH, when combined with cold air in the north, can produce rainband with an east-west zonal distribution in the Yangtze River basin. Overall, the north and east atmospheric forcings make more contributions than the south atmospheric forcing on the generation to the extreme Meiyu in 2020.

The extreme Meiyu in 2020 exhibits obvious QBWO characteristics in the YHRV, and the south atmospheric forcing is crucial for the QBWO of Meiyu. In addition, the contributions of anomalous atmospheric forcings in different directions change with time. Before June 10, the east atmospheric forcing plays a major role in the precipitation evolution. From June 11 to July 3, the precipitation oscillation process is mainly caused by the combined effect of south and north atmospheric forcings. From July 3 to July 10, the north atmospheric forcing is important for the southward precipitation process. After July 10, the atmospheric circulation conditions in 2020 are closer to the climatological mean state, making its rainband evolution also similar to the climatological mean state.

The results also reveal that the upper-level divergence provided by the upper-level westerly jet is not the decisive condition for the strong Meiyu in 2020. There is an interaction between the north cold air, south warm air, Meiyu and upper-level subtropical jet. Only the north atmospheric forcing cannot reproduce the strong westerly jet and Meiyu. The north atmospheric forcing must combine with the south or east atmospheric forcing can reproduce the continuous convergence of the north cold air and south warm air, which intensify the temperature gradient and favors the strong westerly jet and Meiyu. Without the north atmospheric forcing, the westerly jet is weak.

Declarations

Acknowledgements

The authors are grateful to the anonymous reviewers for their valuable comments and suggestions, which significantly improved the manuscript. We acknowledge the Jiangsu Collaborative Innovation Center for Climate Change for their support of this work.

Funding

This work was jointly supported by the National Natural Science Foundation of China (41975090; 41675077), the Natural Science Foundation of Hunan Province, China (2022JJ20043), the science and technology innovation Program of Hunan Province (2022RC1239).

Authors' contributions

Xiaoyu Zhu run the model and analyzed the outputs; Yijia Hu and Xuguang Sun contributed to the idea and structure of the study; Zhong Zhong and Yao Ha performed manuscript review and editing. All authors listed have reviewed the manuscript and approved it for publication.

Ethical Approval

Not available.

Competing interests

The authors declare that they have no competing interests.

Availability of data and materials

The observational reanalysis data as well as initial and lateral boundary conditions used for driving the Regional Climate Model version 4.6 (RegCM4.6) model from the National Centers for Environmental Prediction and National Center for Atmospheric Research (NCEP-NCAR), are available at https://www.esrl.noaa.gov/psd/data/gridded/data.ncep.reanalysis.pressure.html.

The observational precipitation data from the Integrated Multi-satellite Retrievals for Global Precipitation Measurement Mission (IMERG), version 6 (Huffman 2020), are available at https://gpm1.gesdisc.eosdis.nasa.gov/data/GPM_L3/GPM_3IMERGHH.06/.

References

1. Annamalai H, Slingo J (2001) Active/break cycles: Diagnosis of the intraseasonal variability of the Asian summer monsoon. Clim Dyn 18:85-102

2. Chen G, Huang R, Zhou L (2013) Baroclinic instability of the Silk Road pattern induced by thermal damping. J Atmos Sci 70:2875-2893
3. Chen G, Sha W, Iwasaki T, Wen Z (2017) Diurnal cycle of a heavy rainfall corridor over East Asia. Mon Weather Rev 145:3365-3389
4. Chen J, Wen Z, Wu R, Chen Z, Zhao P (2015) Influences of northward propagating 25-90-day and quasi-biweekly oscillations on eastern China summer rainfall. Clim Dyn 45:105-124
5. Chen M, Xie P, Janowiak J, Arkin P (2002) Global land precipitation: A 50-yr monthly analysis based on gauge observations. J Hydrometeor 3:249-266
6. Ding Q, Wang B (2005) Circumglobal teleconnection in the northern hemisphere summer. J Clim 18:3483-3505
7. Ding Y (1992) Summer monsoon rainfalls in China. J Meteor Soc Japan 70:373-396
8. Ding Y (2007) The variability of the Asian summer monsoon. J Meteor Soc Japan 85:21-54
9. Ding Y, Chan J (2005) The East Asian summer monsoon: An overview. Meteorology and Atmospheric Physics 89:117-142
10. Ding Y, Liu Y, Hu Z (2021) The record-breaking mei-yu in 2020 and associated atmospheric circulation and tropical SST anomalies. Adv Atmos Sci 38:1980-1993
11. Ding Y, Liang P, Liu Y, Zhang Y (2020) Multi-scale variability of Meiyu and its prediction: A new review. J Geophys Res 125:e2019JD031496
12. Emanuel K (1991) A scheme for representing cumulus convection in large-dcale models. J Atmos Sci 48:2313-2329
13. Gao X, Shi Y, Han Z, Wang M, Wu J, Zhang D, Xu y, Giorgi F (2017) Performance of RegCM4 over major river basins in China. Adv Atmos Sci 34:441-455
14. Giorgi F, Huang Y, Nishizawa K, Fu C (1999) A seasonal cycle simulation over eastern Asia and its sensitivity to radiative transfer and surface processes. J Geophys Res 104:6403-6424
15. Giorgi F, Coppola E, Solmon F, Mariotti L, Sylla M, Bi X, Elguindi N, Diro G, Nair V, Giuliani G, Turuncoglu U, Cozzini S, Güttler I, O'Brien T, Tawfik A, Shalaby A, Zakey S, Steiner A, Stordal F, Branković Č (2011) RegCM4: Model description and preliminary tests over multiple CORDEX domains. Clim Res 52:7-29
16. Gong D, Ho C (2003) Arctic Oscillation signal in the East Asian summer monsoon. J Geophys Res 108:4066
17. Guan P, Chen G, Zeng W, Liu Q (2020) Corridors of mei-yu-season rainfall over eastern China. J Clim 33:2603-2626
18. He J, Sun C, Liu Y, Matsumoto J, Li W (2007) Seasonal transition features of large-scale moisture transport in the Asian-Australian monsoon region. Adv Atmos Sci 24:1-14
19. Holtslag B, Bruijn E, Pan H (1990) A high-resolution air-mass transformation model for short-range weather forecasting. Mon Weather Rev 118:1561-1575

20. Hoskins B, Ambrizzi T (1993) Rossby wave propagation on a realistic longitudinally varying flow. J Atmos Sci 50:1661-1671
21. Huang C, Li G, Niu J, Zhao F, Zhang H, He Y (2015) A 30-year climatology of the moving-out Tibetan Plateau vortex in summer and its influence on the rainfall in China. J Trop Meteor 31:827-838
22. Huffman GJ (2020) Integrated Multi-satellitE Retrievals for GPM (IMERG) algorithm theoretical basis document (ATBD). NASA/GSFC. https://gpm.nasa.gov/sites/default/files/2020-05/IMERG_ATBD_V06.3.pdf
23. Kemball-Cook S, Wang B (2001) Equatorial waves and air-sea interaction in the boreal summer intraseasonal oscillation. J Clim 14:2923-2942
24. Lawrence D, Oleson K, Flanner M, Thornton P, Swenson S, Lawrence P, Zeng X, Yang Z, Levis S, Sakaguchi K, Bonan G, Slater A (2011) Parameterization improvements and functional and structural advances in version 4 of the Community Land Model. J Adv Model Earth Syst 3:Quarter 1
25. Li C, Wang J, Lin S, Cho H (2004) The relationship between East Asian summer monsoon activity and northward jump of theupper westerly jet location. Chinese J Atmos Sci 28:641-658
26. Li L, Zhang Y (2014) Effects of different configurations of the East Asian subtropical and polar front jets on precipitation during the mei-yu season. J Clim 27:6660-6672
27. Li L, Zhu C, Zhang R, Liu B (2020) Roles of the Tibetan Plateau vortices in the record Meiyu rainfall in 2020. Atmos Sci Lett 22:e1017
28. Liu B, Yan Y, Zhu C, Ma S, Li J (2020) Record-breaking Meiyu rainfall around the Yangtze River in 2020 regulated by the subseasonal phase transition of the North Atlantic Oscillation. Geophys Res Lett 47:e2020GL090342
29. Liu Y, Li W, Ai W (2012) Reconstruction and application of the monthly western Pacific subtropical high indices (in Chinese). J Appl Meteor Climatol 23:414-423
30. Liu Y, Liang P, Sun Y (2019) The Asian summer monsoon: characteristics, variability, teleconnections and projection. Elsevier, Netherlands
31. Lu R, Ren B, Chung H (2005) Differences in annual cycle and 30-60-day oscillations between the summers of strong and weak convection over the tropical western North Pacific. J Clim 18:4649-4659
32. Mao J, Wu G (2006) Intraseasonal variations of the Yangtze rainfall and its related atmospheric circulation features during the 1991 summer. Clim Dyn 27:815-830
33. Ninomiya K (1984) Characteristics of Baiu front as a predominant subtropical front in the summer northern hemisphere. J Meteor Soc Japan 62:880-894
34. Ninomiya K (2000) Large-and meso-α-scale characteristics of Meiyu/Baiu front associated with intense rainfalls in 1-10 July 1991. J Meteor Soc Japan 78:141-157
35. Ninomiya K, Shibagaki Y (2007) Multi-Scale features of the Meiyu-Baiu front and associated precipitation systems. J Meteor Soc Japan 85B:103-122

36. Oh J, Kwon W, Ryoo S (1997) Review of the researches on changma and future observational study (kormex). Adv Atmos Sci 14:207-222
37. Saito N (1985) Quasi-stationary waves in mid-latitudes and the Baiu in Japan. J Meteor Soc Japan 63:983-995
38. Sampe T, Xie S (2010) Large-scale dynamics of the Meiyu-Baiu rainband: Environmental forcing by the westerly jet. J Clim 23:113-134
39. Seo K, Schemm E, Wang W, Kumar A (2007) The boreal summer intraseasonal oscillation simulated in the NCEP Climate Forecast System: The effect of sea surface temperature. Mon Weather Rev 135:1807-1827
40. Song Z, Zhu C, Su J, Liu B (2016) Coupling modes of climatological intraseasonal oscillation in the East Asian summer monsoon. J Clim 29:6363-6382
41. Sun B, Wang H, Wang A, Miao Y, Zhou B, Li H (2021) Regularity and irregularity of the seasonal northward March of the East Asian summer wet environment and the influential factors. J Clim 34:546-566
42. Takaya Y, Ishikawa I, Kobayashi C, Endo H, Ose T (2020) Enhanced Meiyu-Baiu rainfall in early summer 2020: Aftermath of the 2019 super IOD event. Geophys Res Lett 47:e2020GL090671
43. Tao S, Chen L (1987) A review of recent research on the East Asian summer monsoon in China. Monsoon Meteorology, Tallahassee
44. Wang L, Sun X, Yang X, Tao L, Zhang Z (2021) Contribution of water vapor to the record-breaking extreme Meiyu rainfall along the Yangtze River valley in 2020. J Meteor Res 35:557-570
45. Xu Y, Sun X, Yang X (2022) Boreal summer intraseasonal meridional oscillations over East Asia and their influences on precipitation. J Geophys Res 127:e2021JD035779. https://doi.org/10.1029/2021JD035779
46. Yang J, Wang B, Wang B, Bao Q (2010) Biweekly and 21-30-day variations of the subtropical summer monsoon rainfall over the lower reach of the Yangtze River basin. J Clim 23:1146-1159
47. Yang S, Lau W, Kim K (2002) Variations of the East Asian jet stream and Asian-Pacific-American winter climate anomalies. J Clim 15:306-325
48. Zeng X, Zhao M, Dickinson R (1998) Intercomparison of bulk aerodynamic algorithms for the computation of sea surface fluxes using TOGA COARE and TAO data. J Clim 11:2628-2644
49. Zhang R, Sumi A (2002) Moisture circulation over East Asia during El Niño episode in northern winter, spring and autumn. J Meteor Soc Japan 80:213-227
50. Zhang W, Huang Z, Jiang F, Stuecker M, Chen G, Jin F (2021) Exceptionally Persistent Madden-Julian Oscillation Activity Contributes to the Extreme 2020 East Asian Summer Monsoon Rainfall. Geophys Res Lett 48:e2020GL091588

Figures

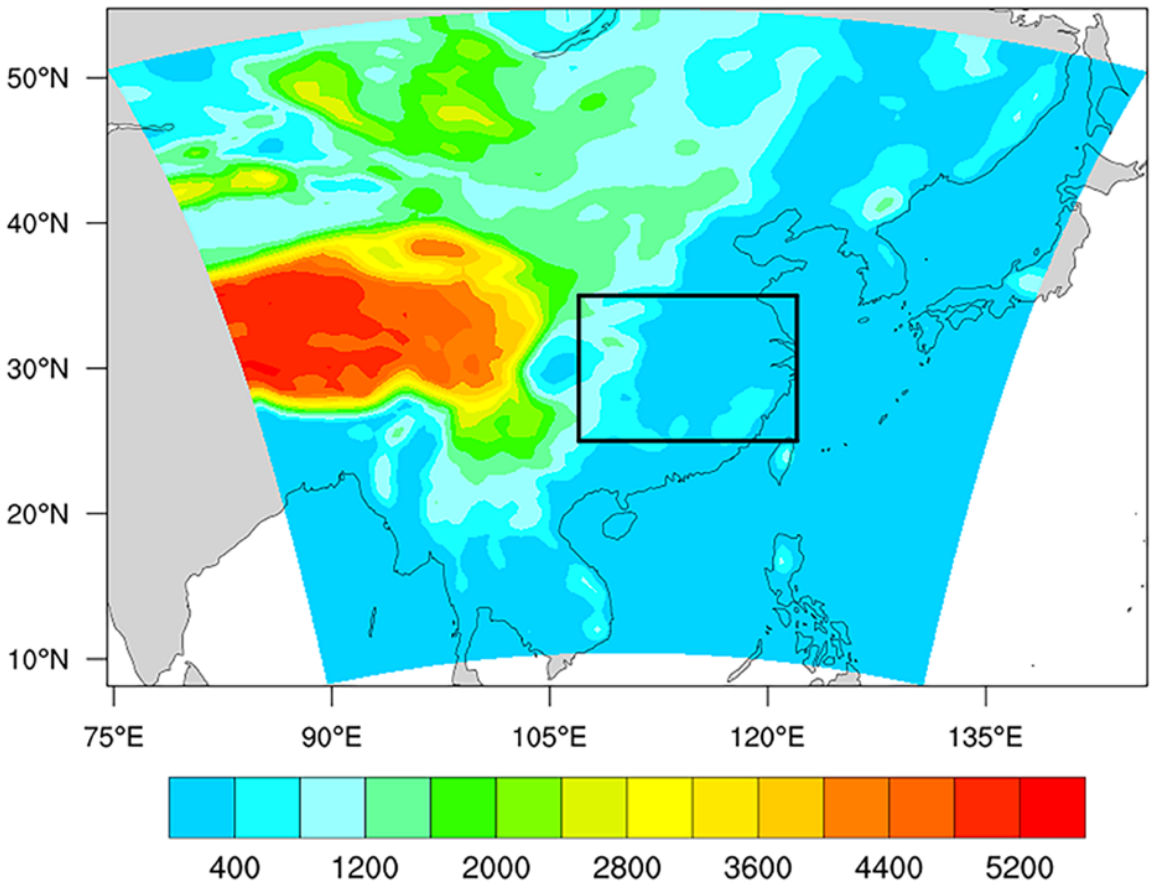

Figure 1

Model domain and distribution of geopotential height (shading, m), where the black rectangle represents the main distribution of rainbands in this extreme Meiyu process (25°N-35°N, 107°E-122°E)

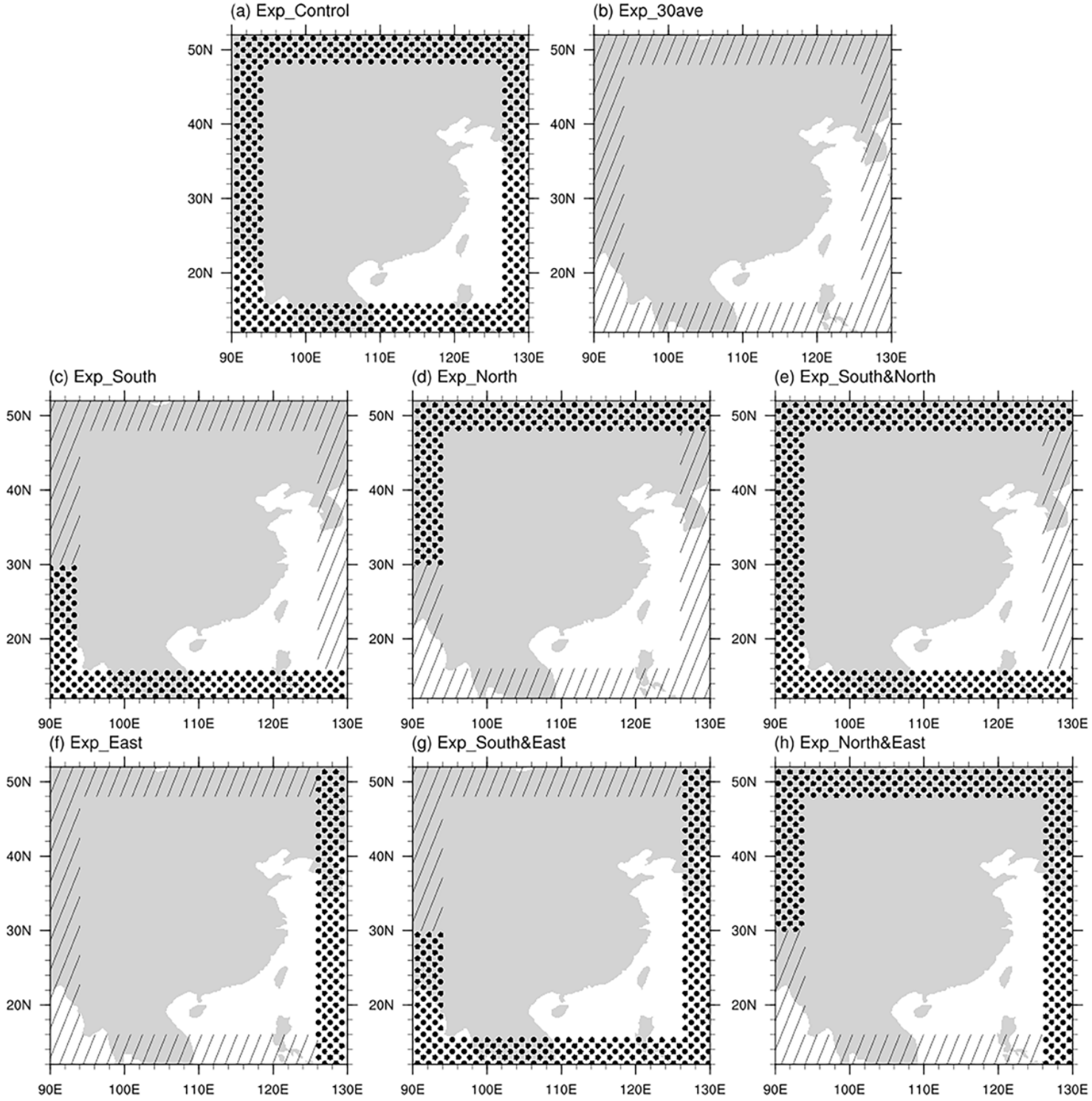

Figure 2

The boundary forcing schematic diagrams of Exp_Control (a) and different sensitivity experiments (Exp_30ave: b; Exp_South: c; Exp_North: d; Exp_South&North: e; Exp_East: f; Exp_South&East: g; Exp_North&East: h) (the dotted areas represent the realistic boundary forcings in 2020, and the diagonal areas represent the 30-year average boundary forcings)

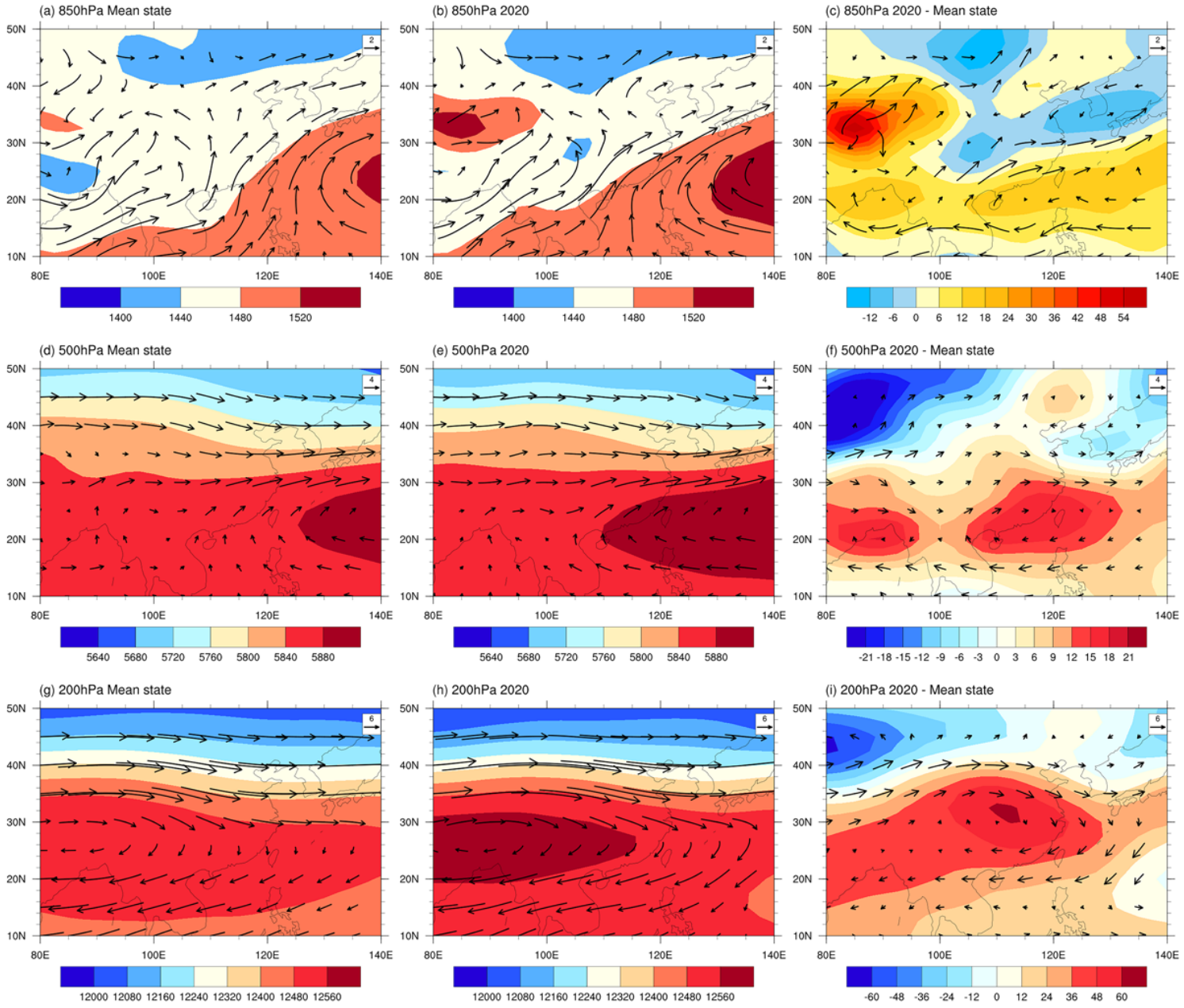

Figure 3

The daily averaged wind vector (vector, m s^{-1}) and geopotential height (shading, gmp) at 850 hPa (a, b and c), 500 hPa (d, e and f), and 200 hPa (g, h and i) for the observed 30-year climatological mean state from 1991 to 2020 (a, d and g), the state in 2020 (b, e and h) and their bias (c, f and i) during June-July

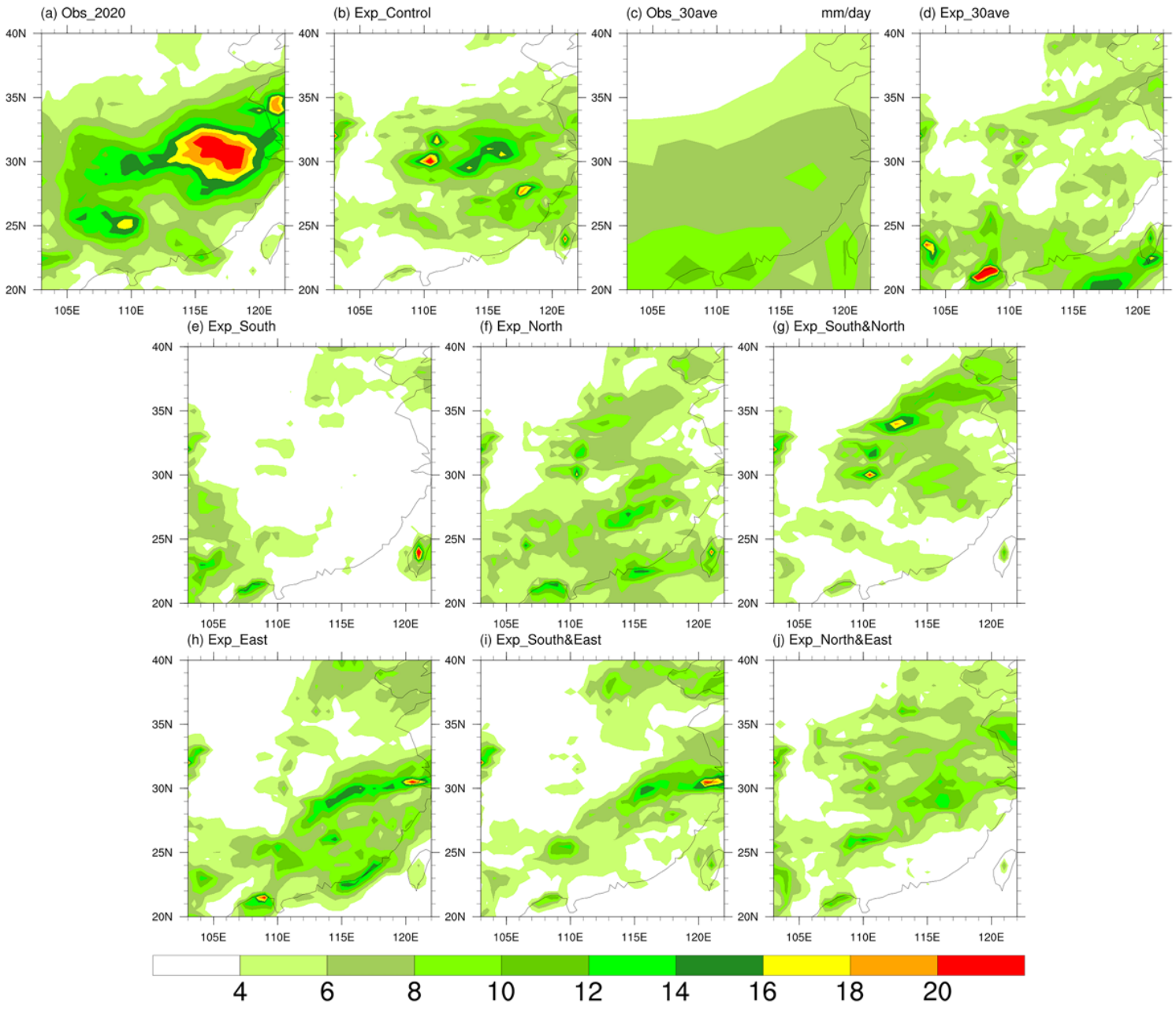

Figure 4

Distributions of the daily averaged precipitation from June to July (shading, mm d^{-1}) in the observations in 2020 (a), Exp_Control (b), the 30-year climatological average data from 1991 to 2020 (c) and different sensitivity experiments (Exp_30ave: d; Exp_South: e; Exp_North: f; Exp_South&North: g; Exp_East: h; Exp_South&East: i; Exp_North&East: j)

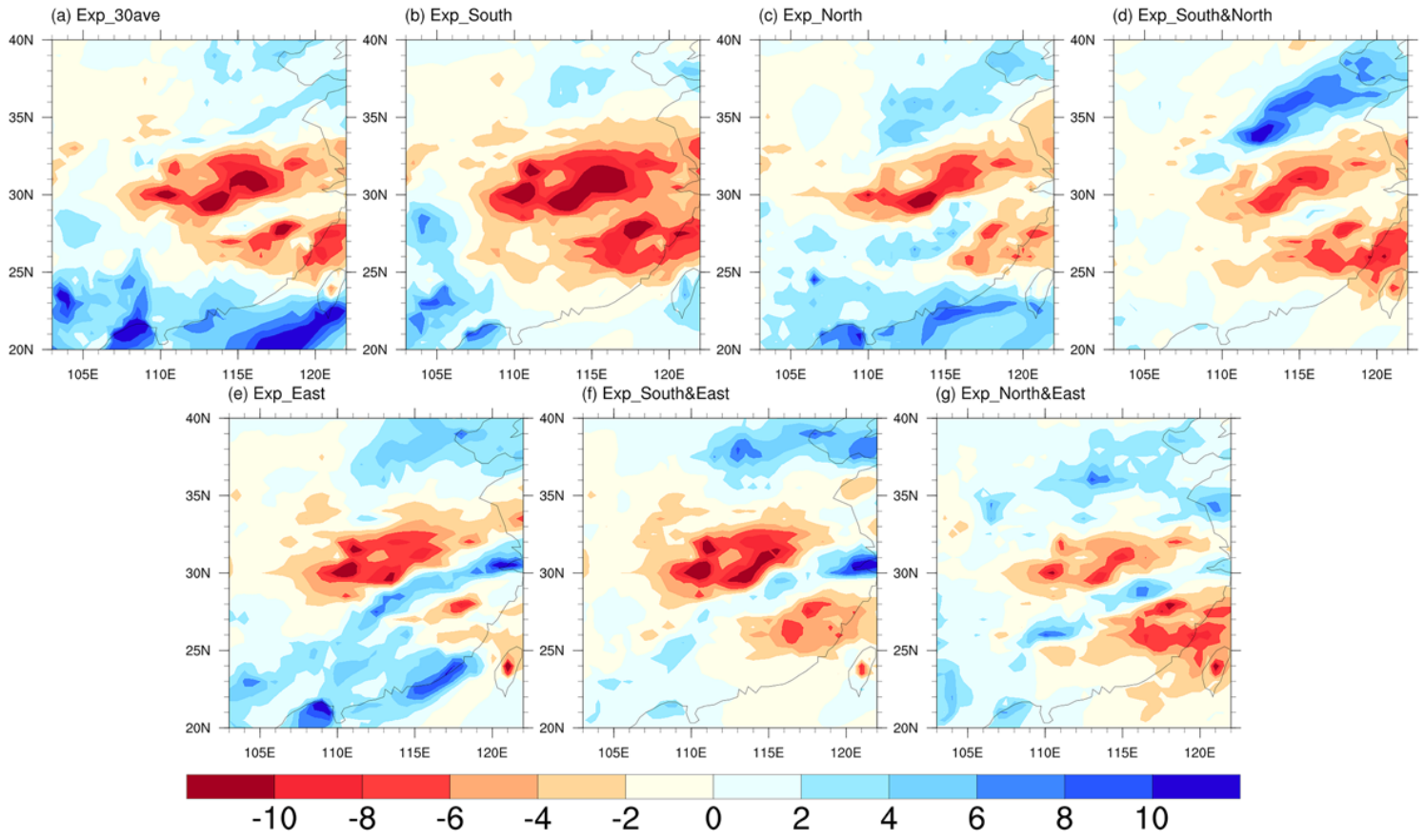

Figure 5

Distributions of the daily averaged precipitation deviations from June to July (shading, mm d^{-1}) between different sensitivity experiments (Exp_30ave: a; Exp_South: b; Exp_North: c; Exp_South_North: d; Exp_East: e; Exp_South&East: f; Exp_North&East: g) minus Exp_Control

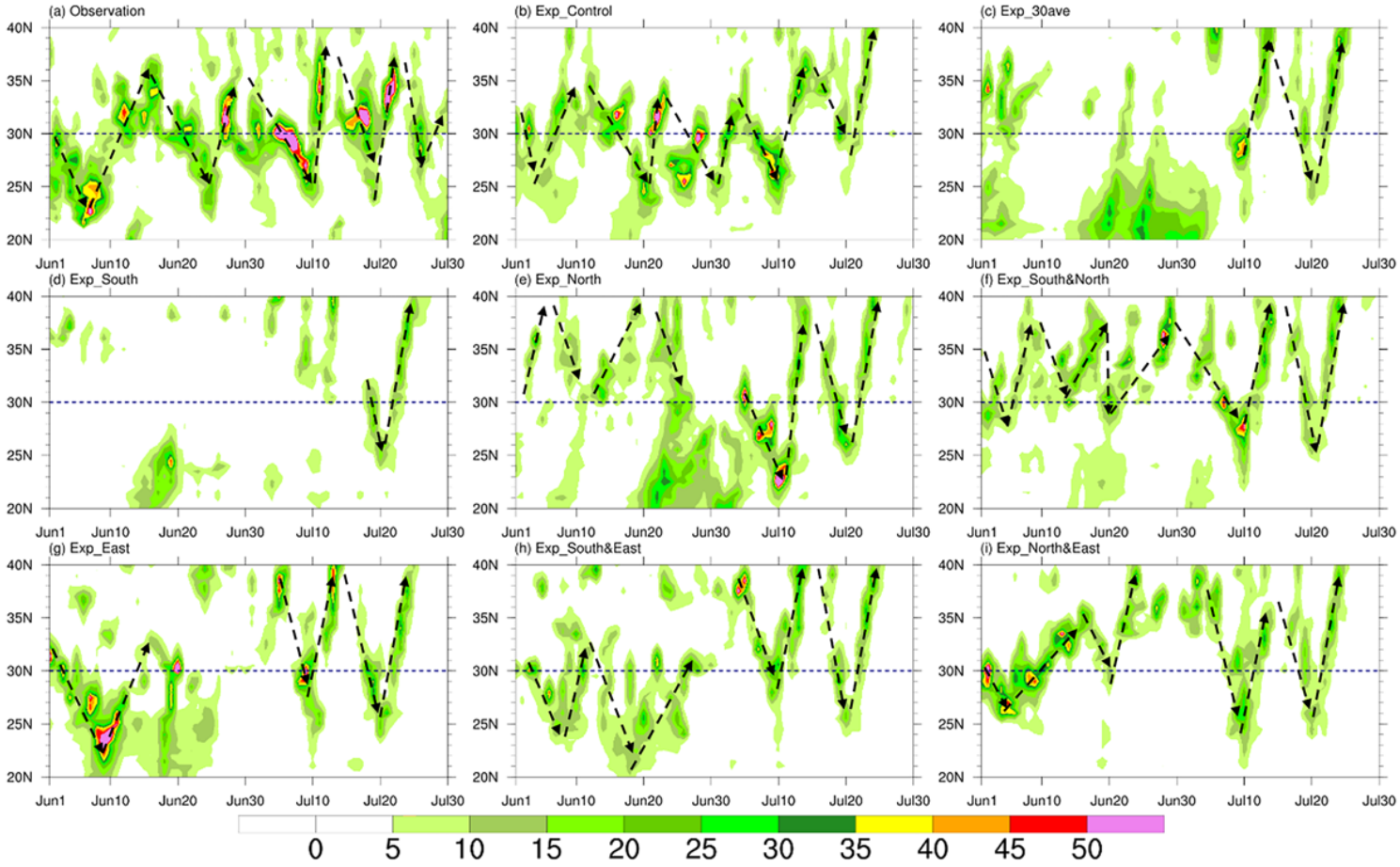

Figure 6

Time-latitude profiles of zonal-averaged (107°-122°E) precipitation from June to July 2020 (shading, mm d^{-1}) in the observations in 2020 (a), Exp_Control (b) and different sensitivity experiments (Exp_30ave: c; Exp_South: d; Exp_North: e; Exp_South&North: f; Exp_East: g; Exp_South&East: h; Exp_North&East: i)

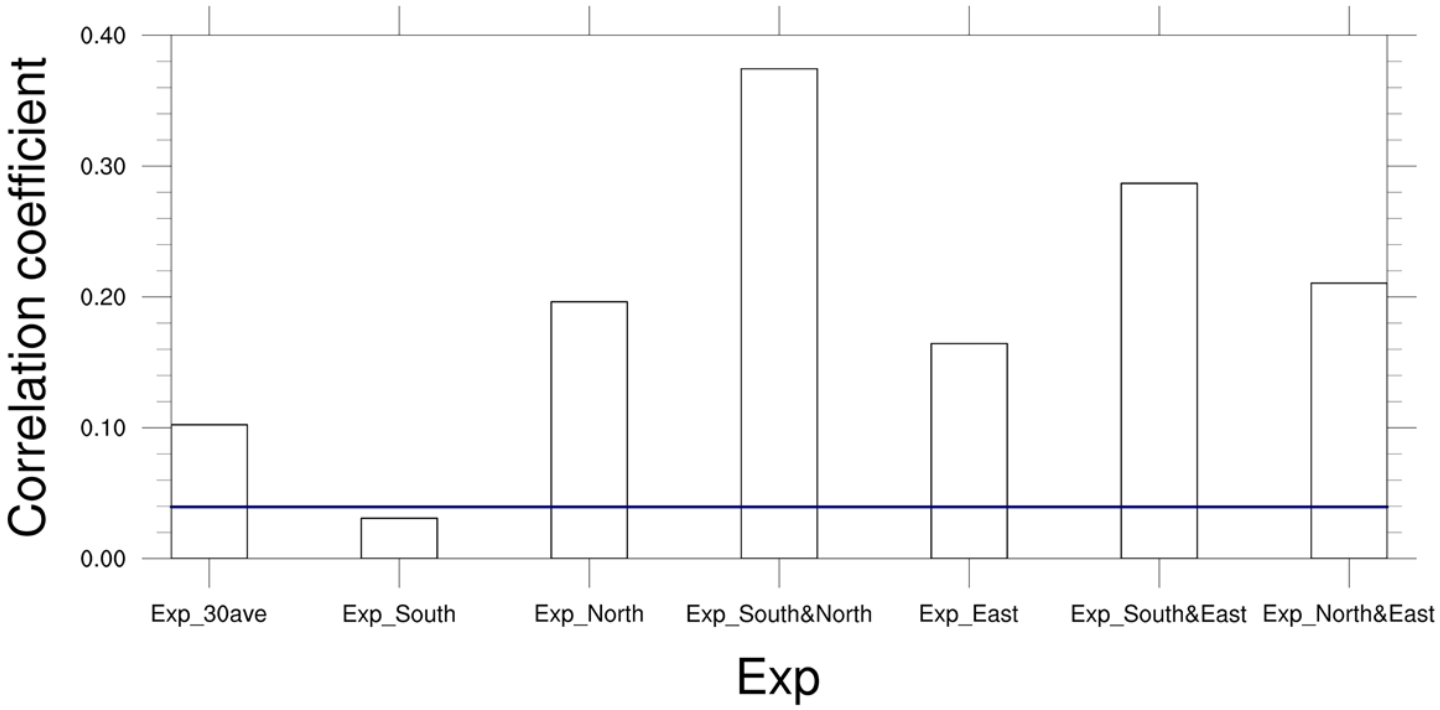

Figure 7

Pattern correlation coefficients between different sensitivity experiments and Exp_Control of time-latitude profiles of zonal-averaged (107°-122°E) precipitation, where the data above the solid blue line are those passing the 95% significance test

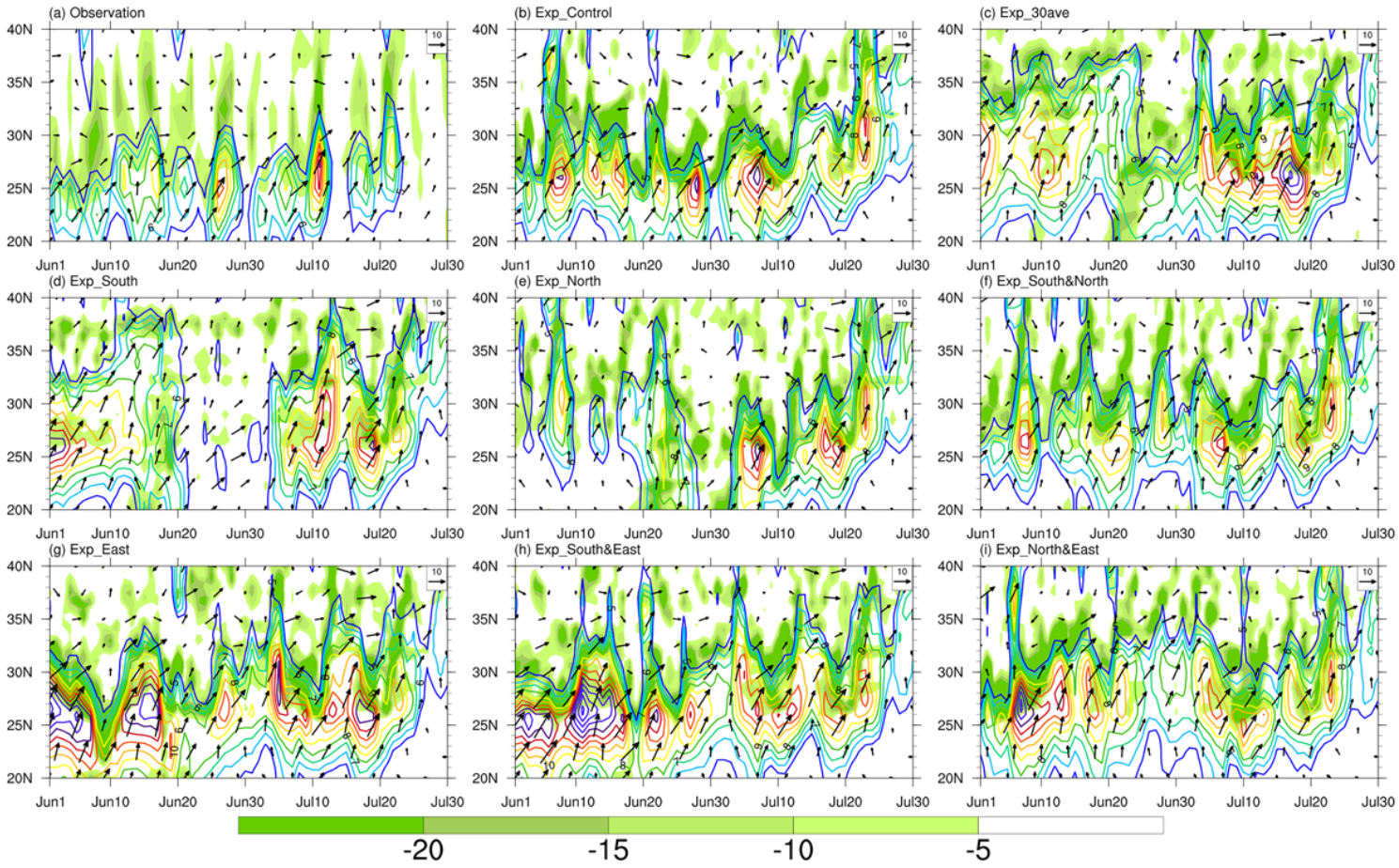

Figure 8

Time-latitude profiles of zonal-averaged (107°-122°E) 850 hPa meridional wind (contour, ≥5 m s^{-1}), horizontal wind (vector, m s^{-1}) and divergence of the vertically integrated water vapor transported from the surface to 300 hPa (shading, 10^{-5} kg m^{-2} s^{-1}) during June to July 2020 in the observations in 2020 (a), Exp_Control (b) and different sensitivity experiments (Exp_30ave: c; Exp_South: d; Exp_North: e; Exp_South&North: f; Exp_East: g; Exp_South&East: h; Exp_North&East: i)

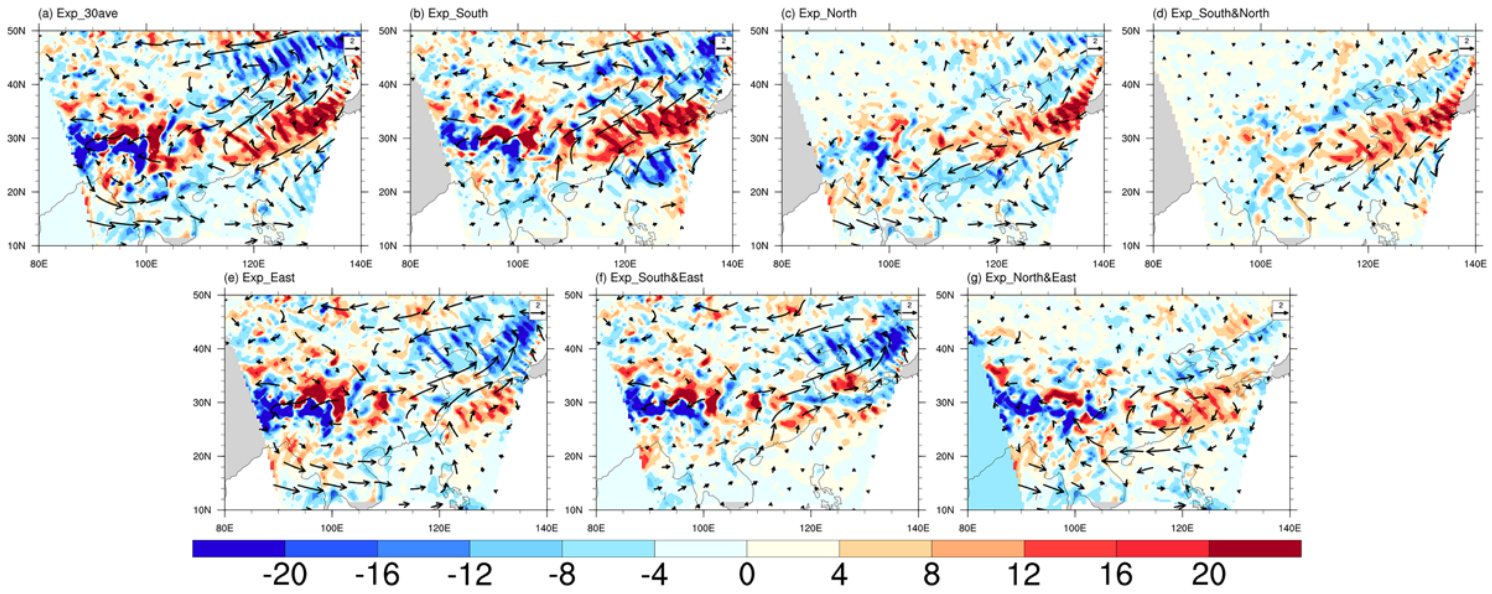

Figure 9

Distributions of daily averaged 850 hPa horizontal wind (vector, m s^{-1}) and divergence of the vertically integrated water vapor transported from the surface to 300 hPa (shading, 10^{-5} kg m^{-2} s^{-1}) deviations during June to July 2020 between different sensitivity experiments (Exp_30ave: a; Exp_South: b; Exp_North: c; Exp_South_North: d; Exp_East: e; Exp_South&East: f; Exp_North&East: g) minus Exp_Control

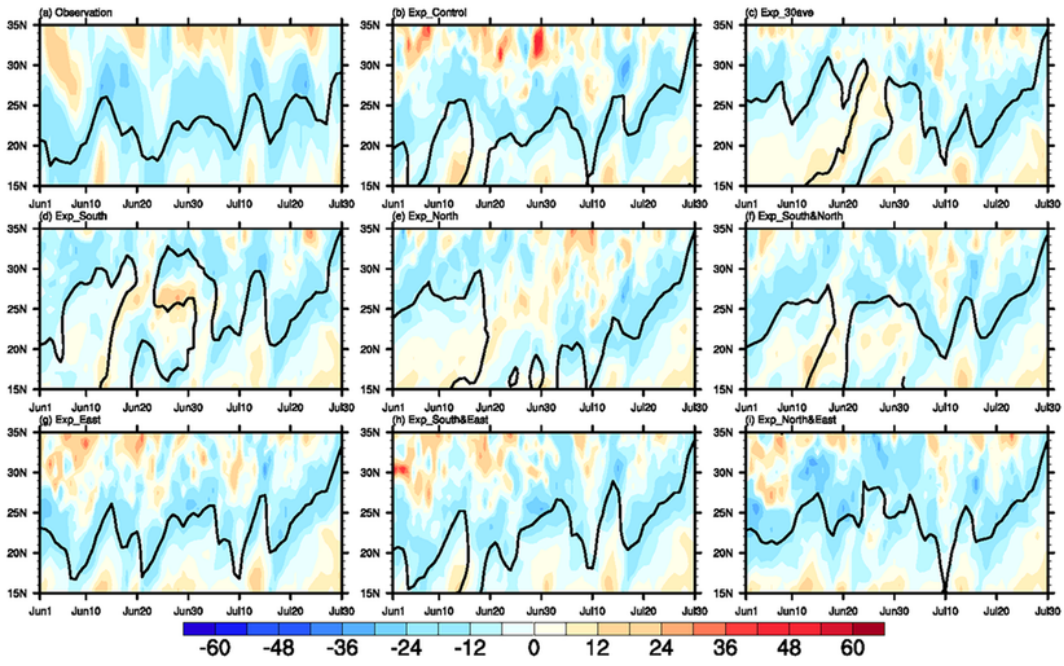

Figure 10

Time-latitude profiles of the zonal-averaged (110°-130°E) ridgeline of the WPSH (contour) and 500 hPa vorticity (shading, 10^{-6} s^{-1}) from June to July 2020 in the observations in 2020 (a), Exp_Control (b) and different sensitivity experiments (Exp_30ave: c; Exp_South: d; Exp_North: e; Exp_South&North: f; Exp_East: g; Exp_South&East: h; Exp_North&East: i)

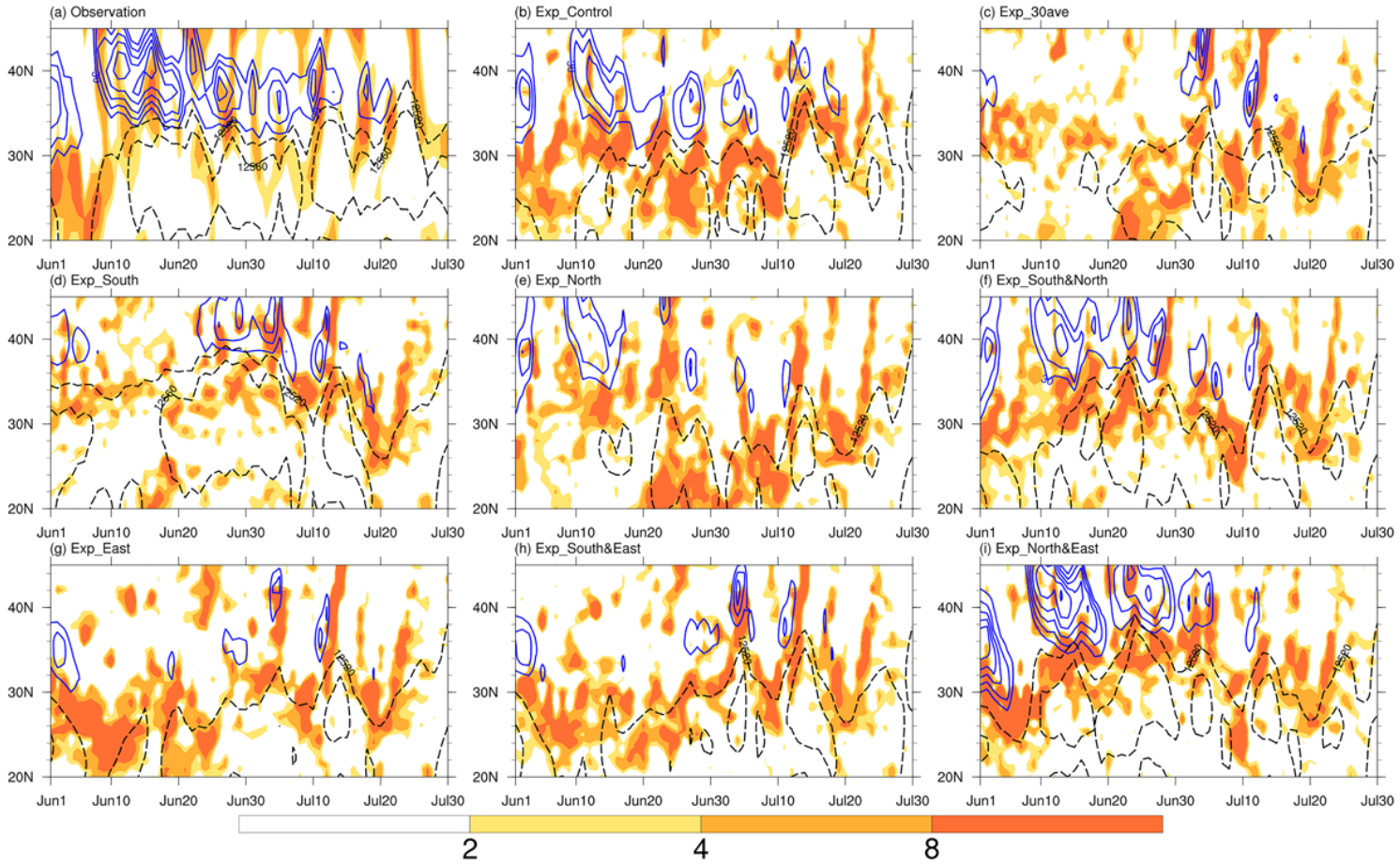

Figure 11

Time-latitude profiles of zonal-averaged (107°-122°E) 200 hPa zonal wind (blue solid lines, ≥30 m s^{-1}), geopotential height (black dashed lines, gpm) and divergence (shading, 10^{-6} s^{-1}) during June to July 2020 in the observations in 2020 (a), Exp_Control (b) and different sensitivity experiments (Exp_30ave: c; Exp_South: d; Exp_North: e; Exp_South&North: f; Exp_East: g; Exp_South&East: h; Exp_North&East: i)